Jugović, D., Mitrić, M., Milović, M., Cvjetićanin, N., Jokić, B., Umićević, A., Uskoković, D., 2017. The influence of fluorine doping on the structural and electrical properties of the LiFePO4 powder. Ceramics International 43, 3224–3230. https://doi.org/10.1016/j.ceramint.2016.11.149

The influence of fluorine doping on the structural and electrical properties of the $LiFePO_4$ powder

Dragana Jugović[a]*, Miodrag Mitrić[b], Miloš Milović[a], Nikola Cvjetićanin[c], Bojan Jokić[d], Ana Umićević[b], Dragan Uskoković[a]

[a]Institute of Technical Sciences of SASA, Knez Mihailova 35/IV, 11 000 Belgrade, Serbia

[b]Vinča Institute of Nuclear Sciences, University of Belgrade, P.O. Box 522, 11 001 Belgrade, Serbia

[c]Faculty of Physical Chemistry, University of Belgrade, Studentski Trg 12-16, P.O. Box 137, Belgrade, Serbia

[d]Faculty of Technology and Metallurgy, University of Belgrade, Karnegijeva 4, 11 000 Belgrade, Serbia

E-mail addresses: dragana.jugovic@itn.sanu.ac.rs (D. Jugović), mmitric@vinca.rs (M. Mitrić), milos.milovic@itn.sanu.ac.rs (M. Milović), nikola.cvj@ffh.bg.ac.rs (N. Cvjetićanin), bjokic@tmf.bg.ac.rs (B. Jokić), umicev@vinca.rs (A. Umićević), dragan.uskokovic@itn.sanu.ac.rs (D. Uskoković)

*Corresponding author: Dragana Jugović

Phone: +381641177549,

Fax: +381112185263,

e-mail: dragana.jugovic@itn.sanu.ac.rs; djugovic@vinca.rs

Abstract

Low intrinsic electronic conductivity is the main disadvantage of $LiFePO_4$ when used as a cathode material in lithium ion batteries. The paper offers experimental proofs of the theoretical prediction that fluorine doping of $LiFePO_4$ can enhance its electrical conductivity. The $LiFePO_4$ and fluorine-doped $LiFePO_4$ olivine type, carbon-free powders are synthesized and examined. The crystal structure refinements in the *Pnma* space group reveal that doping with fluorine ions preserves the olivine structure, while reducing both the lattice parameters and the antisite defect, and increasing the crystallite size. A small amount of incorporated fluorine enhances the electrical conductivity from 4.6×10^{-7} Scm^{-1} to 2.3×10^{-6} Scm^{-1} and has a positive impact on the electrochemical performance. Several spectroscopy techniques (Mössbauer, FTIR, and Raman) reveal differences between the two powders and additionally support the findings of both the Rietveld refinement and the conductivity measurements.

Keywords: A. Powders: solid state reaction; B. Spectroscopy; C. Electrical properties; E. Electrodes;

1. Introduction

The olivine-structured $LiFePO_4$ has been the first material in the orthophosphate family of promising cathode materials for lithium/sodium ion batteries to be examined [1–4]. The most important features of the material include a high energy density (578 $Whkg^{-1}$, a theoretical capacity of 170 $mAhg^{-1}$ and a plateau voltage of 3.4 V vs. Li^+/Li), as well as structural stability, low cost and environmental compatibility [5]. However, despite its advantages, the material suffers from low intrinsic electronic conductivity coupled with low lithium ion diffusivity [5]. These inherent conducting properties have become an obstacle that limits the

application of the material in high-power devices, such as hybrid electric vehicles and electric vehicles. Generally, there are three approaches to overcome this obstacle: (i) the preparation of composites with conductive additives, (ii) particle size minimization and (iii) an ion doping.

The structure of $LiFePO_4$ belongs to the orthorhombic space group *Pnma* (#62), consisting of a slightly distorted hexagonal close-packed (hcp) oxygen framework. The phosphorous atoms occupy 1/8 of tetrahedral sites, while lithium and iron atoms occupy 1/2 of octahedral sites (denoted as M(1) and M(2) sites, respectively). The edge-shared LiO_6 octahedra form linear chains running parallel to the b-axis; FeO_6 forms zigzag planes of corner-shared octahedra in the b-c planes. The PO_4 tetrahedra bridge between adjacent M(2) planes in the olivine structure [1].

Various cations have been widely investigated as dopants in $LiFePO_4$ at Li or Fe sites [6]. On the other hand, there are only several papers dealing with the influence of anion dopants, such as F^-, Cl^-, and S^{2-}, on the properties of $LiFePO_4$ [7–10]. The experimental investigation of fluorine doping was conducted only on the composite powders of $LiFePO_4$ and carbon. In our previous study [11], we investigated in detail the effects of fluorine doping on the crystal structure of $LiFePO_4$ in a carbon composite powder. The obtained powder showed an excellent electrochemical performance with high-rate capability. The careful refinement of X-ray diffraction data indicated that fluorine ions preferred specific oxygen site in the crystal structure, whereas theoretical modeling confirmed and supported the experimental findings, additionally suggesting that F-doping could enhance the material's electric conductivity [11]. Since a carbon coating may mask the investigation of the electrical properties of $LiFePO_4$ it is important to investigate the effect of fluorine doping on carbon-free samples. In the present study we have performed and compared the measurements on carbon-free samples: $LiFePO_4$ and F-doped $LiFePO_4$. It will be shown that fluorine doping of the olivine type $LiFePO_4$ is

feasible only with a small fluorine content. It in turn enhances its conductivity, stabilizes the structure, and has a positive impact on its electrochemical performance.

2. Experimental

2.1. Materials preparation

$LiFePO_4$ was synthesized via aqueous co-precipitation followed by a thermal treatment. Equimolar amounts of $FeSO_4*7H_20$ and $LiNO_3$ were dissolved in a sufficient amount of water. This solution was added drop-wise into an aqueous solution of $(NH_4)_2HPO_4$ under vigorous stirring and heating, when precipitation occurred. After water had evaporated, the obtained precursor powder was calcined at the temperature of 700 °C for 3 hours in a flowing, slightly reductive atmosphere (Ar + 5%H_2). The same procedure was used for the synthesis of the fluorine-doped powder, but this time LiF was used both as lithium and fluorine source. For the convenience, the samples of pure and fluorine-doped $LiFePO_4$ are denoted as LFP and LFPF, respectively.

2.2. Materials characterization

X-ray diffraction data were collected on a Philips PW 1050 diffractometer with Cu-Ka1,2 radiation (Ni filter) at the room temperature. Measurements were done in 2θ range of 10–110° with a scanning step width of 0.02° and 14 s times per step. The crystal structure refinement was based on the Rietveld full profile method [12] using the Koalariet computing program [13].

The ^{57}Fe Mössbauer spectra of the pure and F-doped $LiFePO_4$ samples at 295 K were collected in transmission geometry in a constant acceleration mode using a ^{57}Co(Rh) radioactive source. The spectra were obtained in two velocity ranges: ~ ± 12 mms^{-1} and ~ ± 4.5 mms^{-1}. The velocity scales were calibrated by using α-Fe as the standard material at 295 K. The fitting of the Mössbauer spectra was done with the WinNormos-Site software [14]. The isomer shifts δ are given relative to α-Fe.

The Fourier transform infrared (FTIR) spectra of the samples were recorded in ambient conditions in the mid-IR region (400-4000 cm^{-1}) with a Nicolet IS 50 FT-IR Spectrometer operating in the ATR mode and the measuring resolution of 4 cm^{-1} with 32 scans.

The Raman spectra excited with a diode-pumped solid-state high-brightness laser (532 nm) were collected on a DXR Raman microscope (Thermo Scientific, USA), equipped with an Olympus optical microscope and a CCD detector. The measurements were made at room temperature in the spectral range 100–1800 cm^{-1}. The sample was placed on an X–Y motorized sample stage. The laser beam was focused on the sample using an objective magnification 50 ×. Laser power was kept at 1 mW to prevent the thermal damage of the specimen.

The morphology of the synthesized powder was analyzed by scanning electron microscopy (TESCAN, MIRA3 XMU) at 20 kV.

The particle size analyzer (PSA) Mastersizer 2000 (Malvern Instruments Ltd., UK) was used for the determination of particle size distributions.

The ICP-AES measurements combined with SA720 ion selective electrode (ISE) analysis were used for the elemental analysis of the synthesized powders. The ICP-AES measurements were performed by simultaneous ICP-AES using a Thermo Scientific iCAP-6500 DUO ICP (Thermo Fisher Scientific, UK) spectrometer.

For electrical conductivity measurements, pellets were prepared by die-pressing of the powder with a pressure of 3 tcm^{-2}, and then coating it with Ag paste on both sides. The disc-shaped pellets were around 0.8 cm in diameter and 0.17cm in thickness. Conductivity was measured by aWayne Kerr Universal Bridge B 224 at 1 kHz, at room temperature.

2.3. Electrochemical characterization

Electrochemical measurements were carried out in a closed, argon filled two-electrode cell, with metallic lithium as a counter electrode. 1M solution of $LiClO_4$ (p.a., Chemetall GmbH) in PC (p.a., Honeywell) was used as electrolyte. The working electrodes were made from the synthesized material, carbon black and polyvinylidene fluoride (PVdF, Aldrich) mixed in the 50:40:10 weight percent ratio and deposited on platinum foils from slurry prepared in N-methyl-2- pyrrolidone; the active material content in the electrodes was around 2.8 mg. Galvanostatic charge/discharge tests were performed between 2.3 and 4.1 V at different current rates, at room temperature, by using Arbin BT 2042 battery test system.

3. Results and Discussion

3.1. Morphology studies

Scanning electron microscopy has revealed that there are no great differences in the morphology of the pure and fluorine-doped $LiFePO_4$ powders (Fig. 1). Both powders consist of irregularly shaped particles, highly agglomerated. Particle bonding and neck formation, indicating inter-particle sintering, can be observed as well. Apparently, the morphology of the powder is not affected by fluorine doping. The particle size distribution (PSD) curves of the

powders (Fig. 1) also confirm the observations based on the SEM analysis. PSD curves have a highly uniform lognormal shape, showing the span value of 1.08 and 1.02, and the mean particle size of 391 and 382 nm for LFP and LFPF samples, respectively. It appears that the fluorine-doped $LiFePO_4$ particles are somewhat smaller with a narrower size distribution.

3.2. Electrical conductivity

Electrical conductivity, measured on compacted powders, is slightly higher for the F-doped powder (4.6×10^{-7} Scm^{-1} and 2.3×10^{-6} Scm^{-1} for pure and doped powders, respectively). Having in mind that the carbon-free samples that have been used for the experiments have the same particles size and are also free from any impurity phases (as revealed by XRD, FTIR, and Raman spectroscopy measurements), the measured small difference in electrical conductivity could be ascribed to the effect of fluorine-doping. Theoretical modeling confirms that F-doping can significantly enhance the electric conductivity, but for much higher fluorine content ($LiFePO_{3.75}F_{0.25}$) [11]. The content of fluorine in the synthesized powder is small ($LiFePO_{3.98}F_{0.02}$) and, accordingly, the conductivity improvement is only slight.

3.3. XRD analysis

X-ray diffraction was used for both phase identification and structural analysis. Both samples crystallized in olivine-type $LiFePO_4$ (Fig. 2) with no detectable impurities. The structure of the powders was refined in the space group *Pnma* (D_{2h}^{16}) in the olivine type with the following crystallographic positions: Li^+ ions at the crystallographic position 4*a* [0,0,0] with the local symmetry $\bar{1}$; Fe^{2+} and P^{5+} ions occupied two nonequivalent 4*c* crystallographic positions

[*x*,0.25,*z*] with the local symmetry *m*. Oxygen O^{2-} ions occupied three different crystallographic positions: additional two 4*c* positions and one general 8*d* position [*x*,*y*,*z*] with the local symmetry 1. During the refinement procedure for the fluorine-doped sample, fluorine ions were free to occupy the O(2) sites exclusively, which is in accordance with our previous findings [11], while the total site occupancy of that position for oxygen and fluorine ions was constrained to unity. The Rietveld refinement results indicate that fluorine doping causes the reduction of lattice parameters and the primitive cell volume (Table 1). This indicates that F^- ions are incorporated in the lattice, since the F^- ionic radius is smaller than O^{2-} one ($r^{VI}(F^-)$ = 1.33 Å, $r^{VI}(O^{2-})$ = 1.40 Å [15]). The refined value of the dopant concentration ($LiFePO_{3.98}F_{0.02}$) is much smaller than the nominal fluorine concentration in the precursor powder and it matches well, within the experimental error, with the fluorine concentration obtained by chemical analysis. Apparently, unlike oxide structures [16], the polyanionic PO_4^{3-} structure is more rigid and intolerant to the substitution of oxygen by a fluorine ion, and it only allows for a low level of doping, even when fluorine is present in excess. Doping also leads to an increase of microstructural parameters: crystallite size and microstrain; the fluorine-doped powder is better crystallized.

The Rietveld refinements for both powders have shown an additional electron density on the lithium sites, indicating the formation of the so-called "antisite" defect. This is a defect in which the Li ion (on the M(1) site) and the Fe ion (on the M(2) site) are interchanged, thereby creating a Fe_{Li}^{+}-Li_{Fe}^{-} antisite pair. This antisite disorder (ca. 1-2 mol %) is believed to be an intrinsic property of olivine $LiFePO_4$ [17]. Apparently, fluorine doping lowers the concentration of antisite defects (Table 1). However, it is not possible to distinguish between the creation of the antisite pair $Li_{1-y}Fe_y[Li_yFe_{1-y}]PO_4$ and the existence of both the Fe_{Li}^{+} disorder and lithium deficiency, i.e. $Li_{1-y}Fe_y[\square_yFe_{1-y}]PO_4$, only from Rietveld studies.

Three different types of oxygen atoms form octahedra around Fe and Li atoms and tetrahedra around P atoms. Both fixed and refined fractional atomic coordinates (Table 2) were used for the calculation of all relevant bond distances (Table 3) and bond angles. This enabled us to determine the coordination polyhedra, bond valence sums (Table 2), and the polyhedron's distortion (Table 3). The bond valence sums, V_i, were calculated as a sum of bond valences, s_{ij}, using the equation: $s=\exp[(r_o-r)/B]$, where r_o and B are empirical parameters [18] and r is the bond length from the refined structural model. The average Li–O bond in the fluorine-doped sample is longer than its counterpart in pure $LiFePO_4$, due to which the lithium ion diffusion channel is larger, whereas the Fe–O bond length is shortened. Furthermore, fluorination reduces the distortion of both the Li and P coordination polyhedra, while the Fe octahedron is more distorted. The global instability indexes of 0.2 v.u. indicate the presence of a substantial strain in both structures.

3.4. Mössbauer spectroscopy

The ^{57}Fe Mössbauer spectroscopy is more sensitive to impurities with different valence states of Fe than the diffraction method. In the Mössbauer experiment, we measured the hyperfine interactions of the ^{57}Fe probe nuclei with the surrounding electronic charges. Hence, we had a direct insight into the local ordering, site preference, oxidation states and chemical bonding of Fe atoms.

The Mössbauer spectra of the LFP and LFPF samples observed at low velocity range are presented in Fig. 3. The spectra of LFP and LFPF are similar and they show an apparent symmetry of the velocity lines. The LFP and LFPF Mössbauer spectra in a high velocity range demonstrate features similar to those in a low velocity range and during the fitting procedure there was no indication of the presence of Fe-containing impurity phases in the samples. The final fits of LFP and LFPF Mössbauer spectra included two quadrupole

doublets (denoted as A and B, and A and C, respectively). The fitted hyperfine interaction parameters for both LFP and LFPF (Table 4) indicate that all ^{57}Fe probe ions are in a high-spin state (S = 2) in +2 oxidation state. For both samples, the values of the Mössbauer parameters for the dominant quadrupole doublet A are in a very good agreement with previous measurements [19–24]. This is believed to be associated with the Fe ions positioned at the M(2) regular site within the well ordered $LiFePO_4$ phase (small line width).

The assignment of the minority doublets was done as follows: in case of LFP, the hyperfine parameters for the doublet B reasonably match those provided in the literature data for the Fe ions at the M(1) site [20, 23], though the very large line width indicates a large degree of disorder of this Fe local environment. Also, its relative abundance is in accordance with the XRD observation that 3.7(3) % Fe atoms are allocated at the M(1) site. Contrary to the observations of Li and Shinno [20] and Bini et al. [23], the antisite defect is not well defined in our samples, i.e. it is poorly resolved in the pure material and cannot be observed in the doped material.

The spectrum of the fluorine-doped sample contains two doublets, A and C, with nearly equal isomer shifts, but slightly different quadrupole splittings. The observed isomer shifts for both doublets are consistent with the reported values for the Fe^{2+} iron in the octahedral oxygen coordination [25]. Ferrous iron in the M(2) site would normally be expected to give rise to one doublet. The splitting of the doublet was ascribed to the so-called next-nearest-neighbor (NNN) effect, already identified and examined in the literature [20, 26]. Namely, in the natural triphylite of olivine structures, the substitution of different cations on the M(2) site produces variations in the local next-nearest-neighbor configuration and variable electric field gradients in Fe^{2+} ions. Therefore, multiple doublets with nearly equal isomer shifts but slightly different quadrupole splitting are formed in the Mössbauer spectrum [20]. In our case of fluorine doping, as revealed by the XRD refinement, fluorine ions occupy solely the O(2)

site, which is common for two Li octahedra, one P tetrahedron and one Fe octahedron. Accordingly, the number of the F-containing Fe octahedra (FeO_5F) is equal to the number of fluorine ions, i.e. the fluorine occupancy of the O(2) site, while the number of the only-oxygen-containing octahedra (FeO_6) is equal to the oxygen occupancy of the O(2) site. In the olivine structure, each M(2) octahedron shares corners with four M(2) octahedra (Fig. 4). Five basically different types of next-nearest-neighbor configurations may be distinguished for the iron positioned at the M(2) site and surrounded with oxygen ions only, depending on whether the four adjacent M(2) sites are n FeO_6 octahedra and (4-n) FeO_5F octahedra (n = 0, 1, 2, 3, and 4). The probability of each of these configurations, assuming random distribution and taking into account the occupancies obtained from the Rietveld refinements (c = 0.98, i.e. the oxygen occupation of the O(2) site), are easily calculated using the binomial distribution $\binom{4}{n}c^n(1-c)^{4-n}$ for each configuration (n = 0, 1, 2, 3, and 4). Therefore, the probability of the occurrence of an FeO_6 octahedron surrounded with the same kind of FeO_6 octahedra is calculated by multiplying the aforementioned formula (for n = 4) with c = 0.98. All other instances that include at least one fluorine-containing octahedra (FeO_5F) as the central or next-nearest-neighbor octahedron will give rise to a broad C doublet in the Mössbauer room-temperature spectrum. The obtained probability matches the subspectrum area of the A and C doublets (Table 4). This is another confirmation that fluorine ions solely occupy the O(2) site, as reviled by the Rietveld refinement and predicted by theoretical modeling [11].

3.5. FTIR spectroscopy

Fourier transform infrared spectroscopy (FTIR) is used for the investigation of structures at a local scale. The spectra (Fig. 5) may be divided into two regions: high-frequency bands and low-frequency bands, which are related to the stretching vibrations and the banding

vibrations of the tetrahedral anion, respectively [27]. In between these stretching and bending modes, there is an energy gap extending from 660 to 900 cm^{-1}, the region where vibrations associated with other phosphate anions such as $(P_2O_7)^{4-}$, $(P_3O_{10})^{5-}$ are located [28]. Accordingly, the lack of any structure in this gap indicates that such complexes are not present in the samples. The spectrum of LFPF has sharper and more intense bands with narrower widths and the frequencies of the vibrations show only a small shift (Table 5). These can be ascribed to the improved crystallinity of the powder and a small change of the lattice parameters. Besides that, the spectrum of the F-doped powder is comparable to the FTIR spectrum of the carbon coated olivine type $LiFePO_4$ powders (sharp and intense bands) [29]. Therefore, the differences between the two FTIR spectra of the investigated powders can also be ascribed to a better electrical conductivity of the F-doped sample.

3.6. Raman spectroscopy

The vibrational analysis related to the olivine structure predicts 36 Raman-active fundamentals [30], but the spectrum of $LiFePO_4$ is intrinsically very weak due to the low polarizability of its constituting atoms. The Raman spectra of both samples (Fig. 6) are in good agreement with previous Raman spectroscopic measurements of other $LiMPO_4$ phospho-olivine systems [27, 31]. Raman spectroscopy is a sensitive tool for impurity detection when its amount is well below the detectable limit of XRPD. There are no characteristic bands of Fe_2O_3 in the low-frequency part. Accordingly, the presence of this phase, even on the powder's surface, is excluded. The spectrum of the fluorine-doped sample shows the decrease of the peaks amplitudes with a slight red-shift of their positions. The main features of the spectra are several Raman peaks, observed in the 900–1100 cm^{-1} region, while several weaker peaks are present at lower wavenumbers. One of these peaks, at 951 cm^{-1}, is

much higher in intensity than the others and it is assigned to an essentially symmetric stretching mode (ν_1 of the free ion) [27]. The fitting of the peak in both spectra with the Voigt function reveals that smaller intensities do not have a great influence on the peak width: the full widths at half-maximum are 8.2 and 8.6, for pure and F-doped $LiFePO_4$, respectively. Typically, the depression of the Raman signal, accompanied with the simultaneous line broadening, is observed in samples with a lower degree of crystallinity within the same crystal structure. Having in mind that both powders under investigation are very well crystallized, the origin of the decreased Raman scattering (without line broadening) in the fluorine-doped powder can be associated with its increased conductivity. In addition, during the Raman scattering experiments, the F-doped powder was more sensitive to thermal evolution induced by laser irradiation: when the laser power was raised to 2 mW LFPF, the sample underwent thermal decomposition (visualized in the inset of Figure 6) to Fe_2O_3 and $Li_3Fe_2(PO_4)_3$ [32], while the LFP sample remained intact up to 3 mW. The spectroscopic data suggest that both the dipole moment derivatives (FTIR intensities) and polarizability derivatives (Raman intensities) have changed with fluorine doping without significant impact on the PO_4^{3-} effective force constants (band frequencies).

3.7. Electrochemical performance

The electrochemical properties based on galvanostatic charge–discharge measurements are shown in Fig. 7. Apparently, fluorine has some effect towards the improvement of electrochemical properties. At moderately small current densities, the F-doped material shows a superior electrochemical performance over the undoped material. A smaller voltage gap between the charge and discharge curves for the fluorine-doped sample (Fig. 8) indicates the decrease of the charge transfer resistance due to the conductivity enhancement. However,

at higher current rates, the distinction in the performance under a galvanostatic regime diminishes. X-ray diffraction, Mössbauer, FTIR, and Raman spectroscopy have confirmed that the studied materials are free of impurities and they seem to have similar structures at long and short ranges, whereas the F-doped powder shows a better crystallinity, a lower antisite defect rate, and an increased volume of the lithium diffusion channel. Lithium motion within the olivine crystal structure occurs through one-dimensional channels along the *b* axis [33]. Any defect or impurity that is able to block a channel would prevent the diffusion of the Li ions to all sites in a channel, and would therefore lower the specific capacity of the electrode. The decrease of the antisite defect rate, which was achieved due to fluorine doping, results in a better performance at smaller current densities. However, with an increase of the applied current, low electronic conductivity, in conjunction with large particle sizes, becomes a dominant factor that influences lithium ion diffusion. The electrical conductivity, although slightly higher for the F-doped powder, is still far from the conductivity improvement achieved by carbon coating, and is therefore insufficient to enable faster lithium diffusion.

4. Conclusions

In summary, it can be deduced that fluorine doping of the olivine-type $LiFePO_4$ is feasible only with a small fluorine content within the employed experimental setup, which in turn enhances the electrical conductivity (from 4.6×10^{-7} Scm^{-1} to 2.3×10^{-6} Scm^{-1}) and has a positive impact on the electrochemical performance of the material. X-ray diffraction, Mössbauer, FTIR, and Raman spectroscopy have confirmed that the studied materials are free of impurity phases and appear to be similar in structure at both long and short ranges, while the fluorine-doped powder shows a better crystallinity, a lower antisite defect rate, and an increased volume of the lithium diffusion channel. The crystal structure refinements reveal

that doping with fluorine ions preserves the olivine structure and that it is feasible only for small amounts of fluorine, due to the rigid polyanionic PO_4^{3-} structure. The spectroscopic data suggest that both the dipole moment derivatives (FTIR intensities) and the polarizability derivatives (Raman intensities) change with fluorine doping without significant impact on the PO_4^{3-} effective force constants (band frequencies). The assignment of doublets and the interpretation of area ratios in the Mössbauer room-temperature spectra confirm the finding of the Rietveld refinement: fluorine ions exclusively occupy the O(2) site within the olivine structure. The results presented in this study are promising and they demonstrate that further investigations should be directed towards the synthesis methods that can ensure that a higher content of fluorine is incorporated in the olivine structure.

Acknowledgements

The Ministry of Education, Science and Technological Development of the Republic of Serbia provided financial support for this study under Grants nos. III 45004, III 45015, III 45014, and ON171001.

References

[1] A. K. Padhi, K.S. Nanjundaswamy, J.B. Goodenough, Phospho-olivines as Positive-Electrode Materials for Rechargeable Lithium Batteries, J. Electrochem. Soc. 144 (1997) 1188–1193.

[2] C. Masquelier, L. Croguennec, Polyanionic (phosphates, silicates, sulfates) frameworks as electrode materials for rechargeable Li (or Na) batteries, Chem. Rev. 113 (2013) 6552–6591.

[3] L. Mai, S. Li, Y. Dong, Y. Zhao, Y. Luo, H. Xu, Long-life and high-rate Li3V2(PO4)3/C nanosphere cathode materials with three-dimensional continuous

electron pathways., Nanoscale. 5 (2013) 4864–9.

[4] S. Li, Y. Dong, L. Xu, X. Xu, L. He, L. Mai, Effect of carbon matrix dimensions on the electrochemical properties of Na3V2(PO4)3 nanograins for high-performance symmetric sodium-ion batteries, Adv. Mater. 26 (2014) 3545–3553.

[5] K. Zaghib, A. Guerfi, P. Hovington, A. Vijh, M. Trudeau, A. Mauger, J.B. Goodenough, C.M. Julien, Review and analysis of nanostructured olivine-based lithium recheargeable batteries: Status and trends, J. Power Sources. 232 (2013) 357–369.

[6] J. Wang, X. Sun, Olivine $LiFePO_4$: the remaining challenges for future energy storage, Energy Environ. Sci. 8 (2015) 1110–1138.

[7] F. Lu, Y. Zhou, J. Liu, Y. Pan, Enhancement of F-doping on the electrochemical behavior of carbon-coated $LiFePO_4$ nanoparticles prepared by hydrothermal route, Electrochim. Acta. 56 (2011) 8833–8838.

[8] F. Pan, W. Wang, Synthesis and characterization of core–shell F-doped $LiFePO_4$/C composite for lithium-ion batteries, J. Solid State Electrochem. 16 (2012) 1423–1427.

[9] C.S. Sun, Y. Zhang, X.J. Zhang, Z. Zhou, Structural and electrochemical properties of Cl-doped $LiFePO_4$/C, J. Power Sources. 195 (2010) 3680–3683.

[10] S. Lee, S. Cho, V. Aravindan, H. Kim, Y. Lee, Improved Cycle Performance of Sulfur-Doped $LiFePO_4$ Material at High Temperatures, Bull. Korean Chem. Soc. 30 (2009) 2223.

[11] M. Milović, D. Jugović, N. Cvjetićanin, D. Uskoković, A.S. Milošević, Z.S. Popović, Filip R. Vukajlović, Crystal structure analysis and first principle investigation of F doping in $LiFePO_4$, J. Power Sources. 241 (2013) 70–79.

[12] H.M. Rietveld, A profile refinement method for nuclear and magnetic structures, J.

Appl. Crystallogr. 2 (1969) 65–71.

[13] R.W. Cheary, A. Coelho, A Fundamental Parameters Approach to X-ray Line-Profile Fitting, J. Appl. Crystallogr. (1992) 109–121.

[14] R.A. Brand, WinNormos Mössbauer fitting program, Universität Duisburg, 2008.

[15] R.D. Shannon, Revised effective ionic radii and systematic studies of interatomic distances in halides and chalcogenides, Acta Crystallogr. Sect. A. 32 (1976) 751–767.

[16] P. Yue, Z. Wang, X. Li, X. Xiong, J. Wang, X. Wu, H. Guo, The enhanced electrochemical performance of $LiNi_{0.6}Co_{0.2}Mn_{0.2}O_2$ cathode materials by low temperature fluorine substitution, Electrochim. Acta. 95 (2013) 112–118.

[17] M.S. Islam, D.J. Driscoll, C. A. J. Fisher, P.R. Slater, Atomic-Scale Investigation of Defects, Dopants, and Lithium Transport in the $LiFePO_4$ Olivine-Type Battery Material, Chem. Mater. 17 (2005) 5085–5092.

[18] I.D. Brown, D. Altermatt, Bond-Valence Parameters Obtained from a Systematic Analysis of the Inorganic Crystal Structure Database, Acta Crystallogr. B. 41 (1985) 244–247.

[19] D. Jugović, M. Mitrić, M. Kuzmanović, N. Cvjetićanin, S. Škapin, B. Cekić, V. Ivanovski, D. Uskoković, Preparation of $LiFePO_4$/C composites by co-precipitation in molten stearic acid, J. Power Sources. 196 (2011) 4613–4618.

[20] Z. Li, I. Shinno, Next nearest neighbor effects in triphylite and related phosphate minerals, Mineral. J. 19 (1997) 99–107.

[21] A.S. Andersson, B. Kalska, L. Haggstrom, J.O. Thomas, Lithium extraction/insertion in $LiFePO_4$: An X-ray diffraction and Mössbauer spectroscopy study, Solid State Ionics. 130 (2000) 41–52.

[22] M. Maccario, L. Croguennec, A. Wattiaux, E. Suard, F. Le Cras, C. Delmas, C-containing $LiFePO_4$ materials - Part I: Mechano-chemical synthesis and structural characterization, Solid State Ionics. 179 (2008) 2020–2026.

[23] M. Bini, S. Ferrari, D. Capsoni, P. Mustarelli, G. Spina, F. Del Giallo, M. Lantieri, C. Leonelli, A. Rizzuti, V. Massarotti, Pair distribution function analysis and Mössbauer study of defects in microwave-hydrothermal $LiFePO_4$, RSC Adv. 2 (2012) 250.

[24] L. Aldon, A. Perea, 2D-correlation analysis applied to in situ and operando Mössbauer spectroscopy, J. Power Sources. 196 (2011) 1342–1348.

[25] A.G. Maddock, Mössbauer spectroscopy, Principles and Applications of the Techniques, Horwood Publishing Limited, Chichester, England, 1997.

[26] E. Dowry, D.H. Lindsley, Mossbauer Spectra of Synthetic Hedenbergite-ferrosilite Pyroxenes, Am. Mineral. 58 (1973) 850–868.

[27] M.T. Paques-Ledent, P. Tarte, Vibrational studies of olivine-type compounds—II Orthophosphates, -arsenates and -vanadates $A^{I}B^{II}X^{V}O_4$, Spectrochim. Acta Part A Mol. Spectrosc. 30 (1974) 673–689.

[28] A. Hezel, S. Ross, The vibrational spectra of some divalent metal pyrophosphates, Spectrochim. Acta - Part A Mol. Spectrosc. 23 (1967) 1583–1589.

[29] M. Maccario, L. Croguennec, B. Desbat, M. Couzi, F. Le Cras, L. Servant, Raman and FTIR Spectroscopy Investigations of Carbon-Coated Li_xFePO_4 Materials, J. Electrochem. Soc. 155 (2008) A879.

[30] M.T. Paques-Ledent, P. Tarte, Vibrational studies of olivine-type compounds—I. The i.r. and Raman spectra of the isotopic species of Mg_2SiO_4, Spectrochim. Acta Part A Mol. Spectrosc. 29 (1973) 1007–1016.

[31] W. Paraguassu, P.T.C. Freire, V. Lemos, S.M. Lala, L. A. Montoro, J.M. Rosolen,

Phonon calculation on olivine-like $LiMPO_4$ (M = Ni, Co, Fe) and Raman scattering of the iron-containing compound, J. Raman Spectrosc. 36 (2005) 213–220.

[32] E. Markevich, R. Sharabi, O. Haik, V. Borgel, G. Salitra, D. Aurbach, G. Semrau, M.A. Schmidt, N. Schall, C. Stinner, Raman spectroscopy of carbon-coated $LiCoPO_4$ and $LiFePO_4$ olivines, J. Power Sources. 196 (2011) 6433–6439.

[33] D. Morgan, a. Van der Ven, G. Ceder, Li Conductivity in Li_xMPO_4 (M = Mn, Fe, Co, Ni) Olivine Materials, Electrochem. Solid-State Lett. 7 (2004) A30.

Figure captions

Fig. 1. FESEM micrographs of the $LiFePO_4$ powder (left) and the fluorine-doped $LiFePO_4$ powder (right), and the corresponding particle size distributions for $LiFePO_4$ (red line) and fluorine-doped $LiFePO_4$ (black line).

Fig. 2. The observed (•), calculated (-), and the difference between the observed and calculated (bottom) X-ray diffraction data taken at room temperature for $LiFePO_4$ (up) and fluorine-doped $LiFePO_4$ (down). The vertical markers below the diffraction patterns indicate the positions of possible Bragg reflections for the olivine-type $LiFePO_4$.

Fig. 3. The Mössbauer spectra of $LiFePO_4$ (a) and fluorine-doped $LiFePO_4$ (b) at room temperature. The symbols correspond to the experimental data and the red line to the total fitting. The red solid line in the lower part of the plot represents the difference between the experimental and total fitted spectrum. The fitted lines of the Mössbauer subspectra are plotted above the experimental spectrum (blue – doublet A, magenta – doublet B, and olive – doublet C).

Fig. 4. A motif of one FeO_6 octahedron corner-connected to four FeO_6 neighboring octahedra. The O(2) site is occupied by an oxygen or fluorine ion.

Fig. 5. FTIR spectra of $LiFePO_4$ (black line) and fluorine-doped $LiFePO_4$ (red line).

Fig. 6. Raman spectra of $LiFePO_4$ (bottom) and fluorine-doped $LiFePO_4$ (top). In the inset is Raman spectrum of fluorine-doped $LiFePO_4$ after thermal degradation when the laser power was raised to 2 mW.

Fig. 7. Discharge curves of $LiFePO_4$ (black solid line) and fluorine-doped $LiFePO_4$ (red dashed line) at different current rates and the rate performance (inset).

Fig. 8. The charge-discharge curves of $LiFePO_4$ (black solid line) and fluorine-doped $LiFePO_4$ (red dashed line) at 0.2C current rate.

Table 1. The main results of the Rietveld refinements.

	$LiFePO_4$	F-doped $LiFePO_4$
Lattice parameters (Å)	a = 10.3342(3) b = 6.0076(2) c = 4.6942(2)	a = 10.3324(4) b = 6.0074(2) c = 4.6926(2)
Primitive cell volume ($Å^3$)	V = 291.44(2)	V = 291.27(2)
Mean crystallite size (nm)	128(5)	141(7)
Microstrain (%)	0.00(1)	0.08(1)
Li site occ. by Fe	0.037(3)	0.014(3)
O2 site occ. by F	-	0.02(1)
R factor (%)	Rwp = 1.4	Rwp = 1.3

Table 2. Fixed and refined fractional atomic coordinates, bond valence sums (V*i*), and isotropic displacement parameters (B).

Fractional coordinates	Pure $LiFePO_4$			V_i	F-doped $LiFePO_4$			V_i	B ($Å^2$)
	x	y	z	(v.u.)	x	y	z	(v.u.)	
Li (4*a*)	0	0	0	0.991	0	0	0	0.959	2.5
Fe (4*c*)	0.2823(2)	0.25	0.9734(5)	1.986	0.2822(2)	0.25	0.9733(6)	2.030	0.5
P (4*c*)	0.0952(4)	0.25	0.4195(9)	4.577	0.0961(4)	0.25	0.4146(9)	4.587	0.4
O(1) (4*c*)	0.0987(9)	0.25	0.7445(1)	1.871	0.0976(9)	0.25	0.7412(16)	1.833	2.1
O(2) (4*c*)	0.4530(12)	0.25	0.2176(10)	1.804	0.4514(10)	0.25	0.2101(11)	1.806	2.1
O(3) (8*d*)	0.1654(7)	0.0453(10)	0.2796(10)	1.939	0.1660(8)	0.0434(12)	0.2794(10)	1.955	2.1

Table 3. Selected M-O distances (in Å) and the distortions of MO_n polyhedra in $LiFePO_4$ and fluorine-doped $LiFePO_4$.

M – O bond	$LiFePO_4$	F-doped $LiFePO_4$
Fe – O(1)	2.1807	2.1963
Fe – O(2)	2.1041	2.0717
Fe – O(3) x 2	2.2448	2.2458
Fe – O(3)' x 2	2.0655	2.0547
$(Fe – O)_{ave}$	2.1509	2.1448
FeO_6 distortion	1.3×10^{-3}	1.6×10^{-3}
Li – O(1) x 2	2.1758	2.1789
Li – O(2) x 2	2.0612	2.0877
Li – O(3) x 2	2.1722	2.1746
$(Li – O)_{ave}$	2.1364	2.1471
LiO_6 distortion	6.2×10^{-4}	3.8×10^{-4}
P – O(1)	1.5262	1.5328
P – O(2)	1.6040	1.6055
P – O(3) x 2	1.5713	1.5696
$(P – O)_{ave}$	1.5682	1.5694
PO_4 distortion	3.1×10^{-4}	2.7×10^{-4}

Table 4. Mössbauer parameters for pure and F-doped $LiFePO_4$ at room temperature: the line width Γ; the isomer shift δ (relative to α-Fe); the quadrupole splitting ΔE_Q in case of pure electric interaction; relative area of subspectrum A. The errors given in parenthesis are from the fitting procedure only.

Sample	Doublet	Γ (mms^{-1})	δ (mms^{-1})	ΔE_Q (mms^{-1})	A (%)	site	Assignment	Probability
$LiFePO_4$	A	0.275(2)	1.234(1)	2.962(1)	96.1(3)	Fe^{2+} (O_h)	M(2)	
	B	1.3(5)	1.0(1)	1.5(3)	3.9(5)	Fe^{2+} (O_h)	M(1)	
F-doped $LiFePO_4$	A	0.291(3)	1.239(1)	2.963(1)	89.5(7)	Fe^{2+} (O_h)	M(2)	0.904
	C	1.0(1)	1.22(3)	2.6(1)	10.5(8)	Fe^{2+} (O_h)	M(2) influenced by F ion	0.096

Table 5. Observed FTIR bands in $LiFePO_4$ and fluorine-doped $LiFePO_4$.

LFP bands (cm^{-1})	LFPF bands (cm^{-1})	Δ (cm^{-1})	Assignment [27]
1138	1139	-1	ν3
1094	1094	0	ν3
1050	1052	-2	ν3
966	966	0	ν3
945	946	-1	ν1
636	636	0	ν4
578	578	0	ν4 + ν2
549	550	-1	ν4 + ν2
497	498	-1	ν4 + ν2
465	465	0	ν4 + ν2

Figure 1.

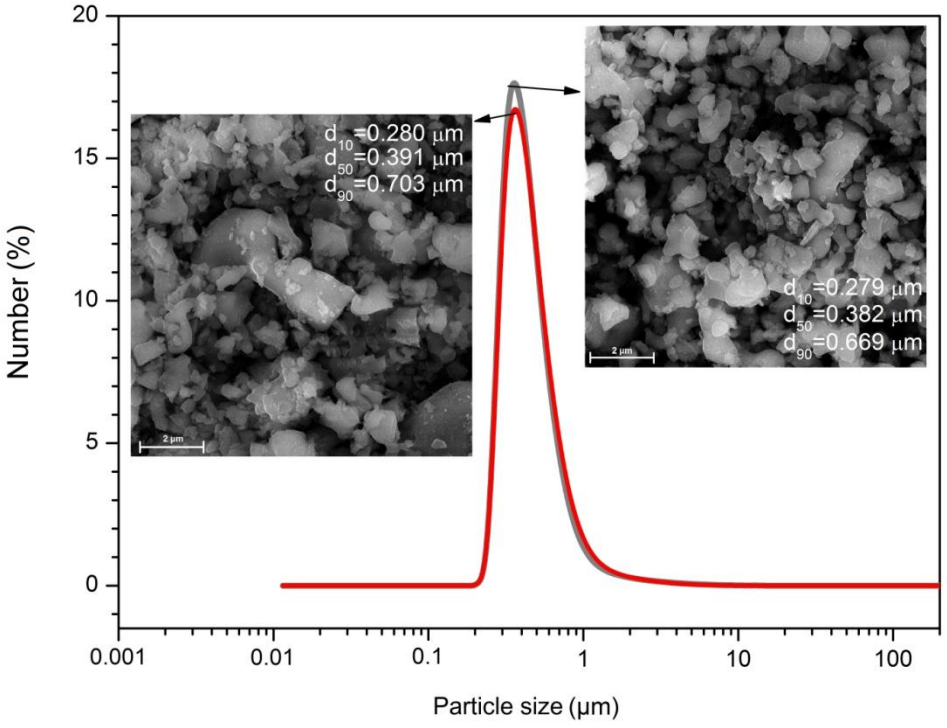
Number (%)
Particle size (μm)
0
5
10
15
20
0.001
0.01
0.1
1
10
100
d10=0.280 μm
d50=0.391 μm
d90=0.703 μm
d10=0.279 μm
d50=0.382 μm
d90=0.669 μm

Figure 2.

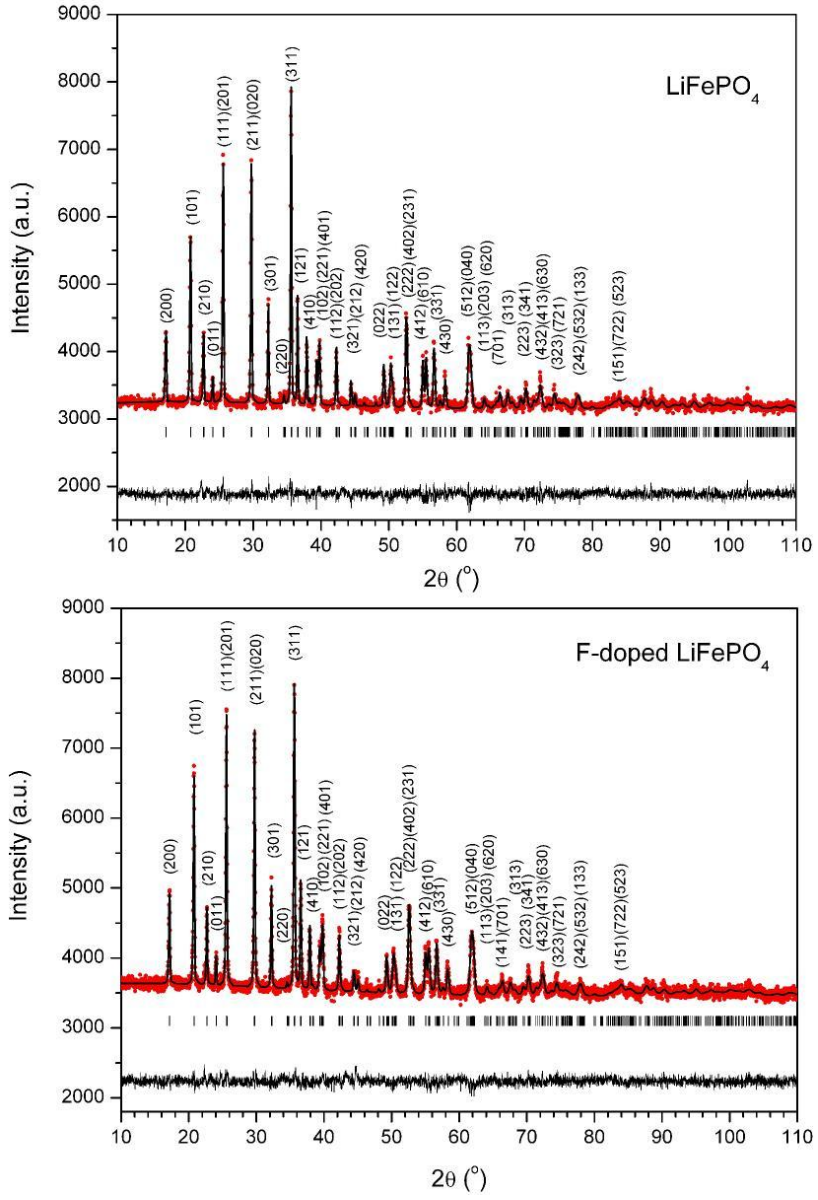
LiFePO4
F-doped LiFePO4
Intensity (a.u.)
2θ (°)
(200)
(101)
(210)
(011)
(111)(201)
(211)(020)
(301)
(220)
(311)
(121)
(410)
(102)(221)(401)
(112)(202)
(321)(212)(420)
(022)
(131)(122)
(222)(402)(231)
(412)(610)
(331)
(430)
(512)(040)
(113)(203)(620)
(701)
(313)
(223) (341)
(432)(413)(630)
(323)(721)
(242)(532)(133)
(151)(722) (523)

Figure 3.

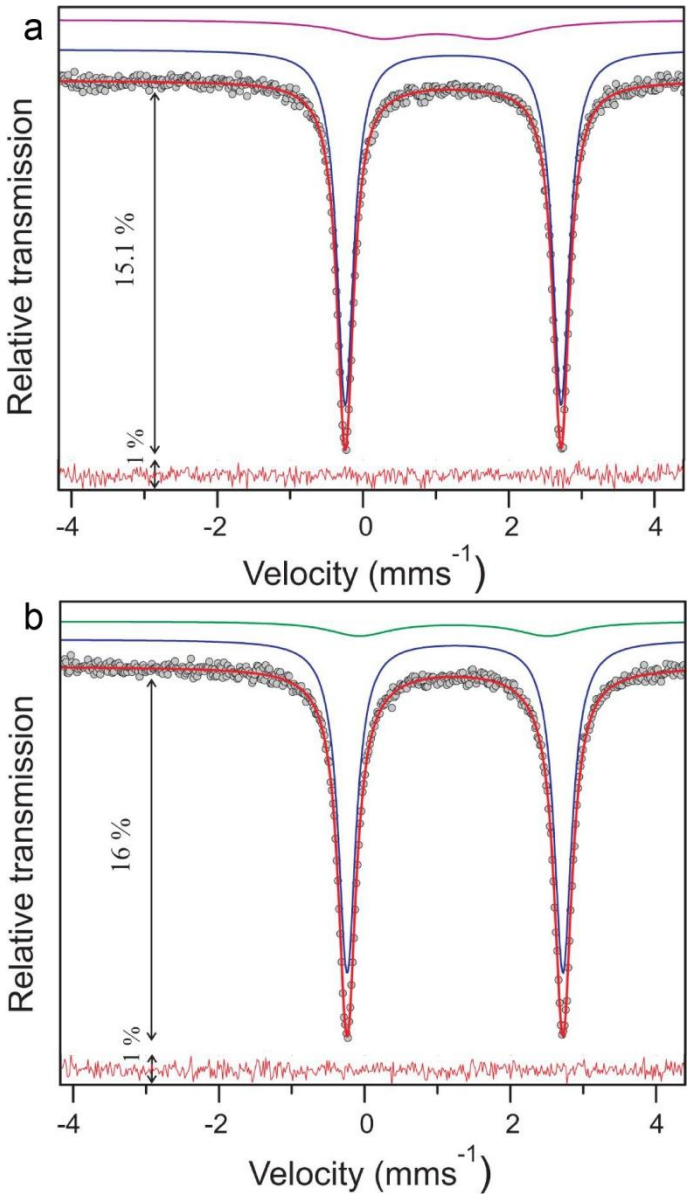
a
Relative transmission
15.1 %
1 %
-4
-2
0
2
4
Velocity (mms-1)
b
Relative transmission
16 %
1 %
-4
-2
0
2
4
Velocity (mms-1)

Figure 4.

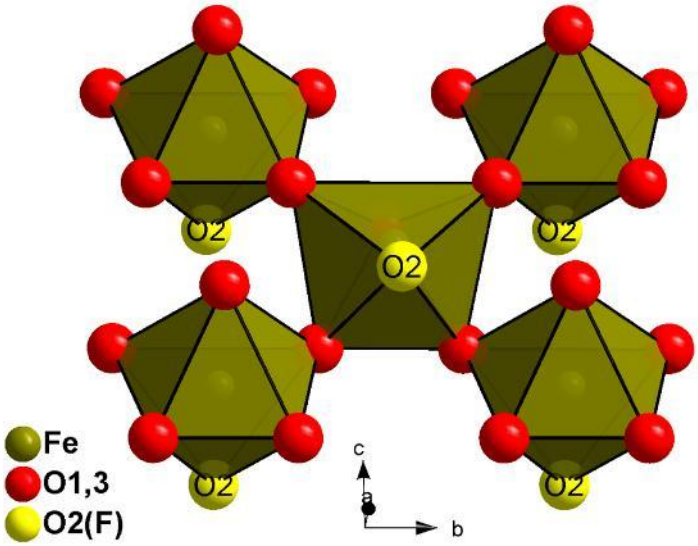

Figure 5.

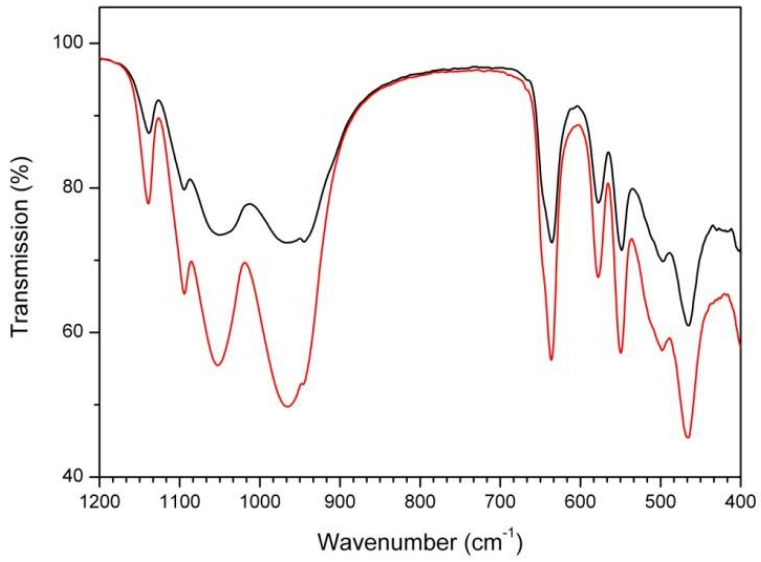

Figure 6.

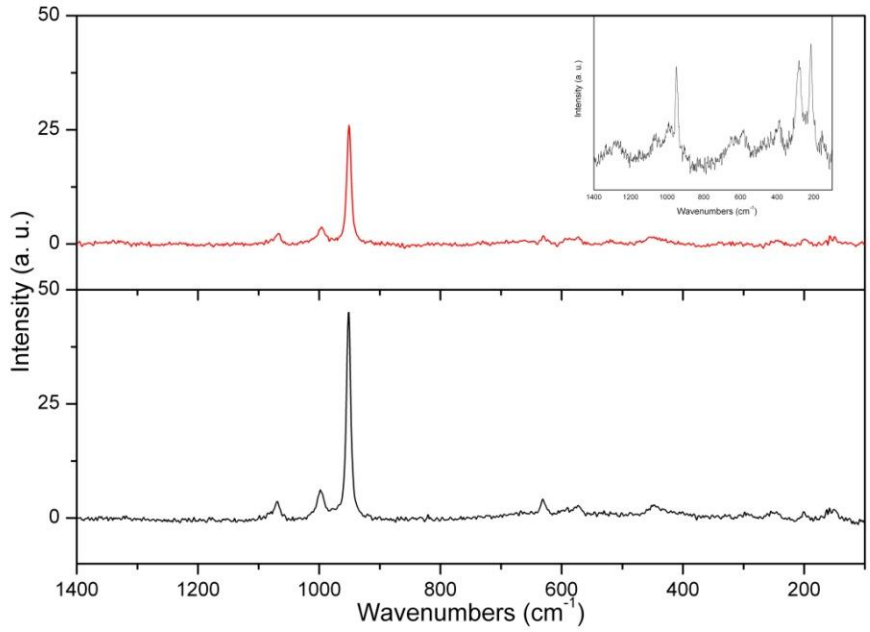

Figure 7.

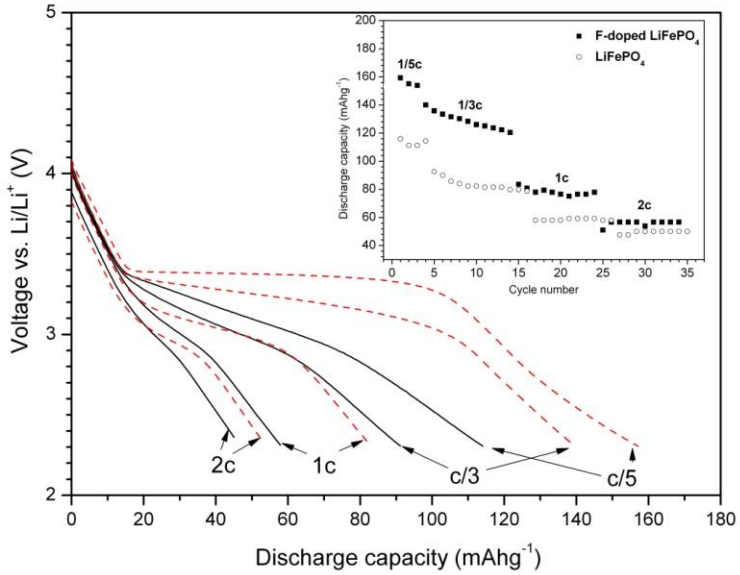

Figure 8.